ELSEVIER

Tectonophysics 275 (1997) 221–241

TECTONOPHYSICS

Deep structure of Medicine Lake volcano, California

Joachim R.R. Ritter [a,*], John R. Evans [b]

[a] *Geophysical Institute, University of Karlsruhe, Hertzstr. 16, 76187 Karlsruhe, Germany*
[b] *U.S. Geological Survey, 345 Middlefield Rd., MS-977, Menlo Park, CA 94025, USA*

Received 17 December 1995; accepted 20 August 1996

Abstract

Medicine Lake volcano (MLV) in northeastern California is the largest-volume volcano in the Cascade Range. The upper-crustal structure of this Quaternary shield volcano is well known from previous geological and geophysical investigations. In 1981, the U.S. Geological Survey conducted a teleseismic tomography experiment on MLV to explore its deeper structure. The images we present, calculated using a modern form of the ACH-inversion method, reveal that there is presently no hint of a large (>100 km^3), hot magma reservoir in the crust. The compressional-wave velocity perturbations show that directly beneath MLV's caldera there is a zone of increased seismic velocity. The perturbation amplitude is +10% in the upper crust, +5% in the lower crust, and +3% in the lithospheric mantle. This positive seismic velocity anomaly presumably is caused by mostly subsolidus gabbroic intrusive rocks in the crust. Heat and melt removal are suggested as the cause in the upper mantle beneath MLV, inferred from petro-physical modeling. The increased seismic velocity appears to be nearly continuous to 120 km depth and is a hint that the original melts come at least partly from the lower lithospheric mantle. Our second major finding is that the upper mantle southeast of MLV is characterized by relatively slow seismic velocities (−1%) compared to the northwest side. This anomaly is interpreted to result from the elevated temperatures under the northwest Basin and Range Province.

Keywords: seismic tomography; lithosphere; volcano; Cascades

1. Introduction

Although numerous geological, petrological, and geophysical studies have dealt with Medicine Lake volcano (MLV, Fig. 1), its structure below the upper crust is still poorly known. Our teleseismic tomography study yields information about the volcano's deep structure for the first time. Images display perturbations of the compressional-wave velocity down to 120 km depth; the data for these results are measured travel-time residuals for P, ScP, and PKPdf phases of teleseisms (Aki et al., 1977). Similar experiments in other active volcanic regions (cf. Iyer and Dawson, 1993) have demonstrated the utility of this technique. Silicic magma chambers in the crust have been imaged as low-velocity zones (cf. Dawson et al., 1990; Lutter et al., 1995). The magmatic relationship and structural connection of crustal volcanic features to deeper mantle anomalies has also been revealed (Evans, 1982a; Ritter et al., 1995). Recent low-resolution, regional teleseismic tomography models for the western United States show that some volcanoes (e.g., MLV or Mt. Shasta in Cali-

* Corresponding author. Tel.: +49 721-6084-486. Fax: +49 721-71173. E-mail: ritter@gpiwap3.physik.uni-karlsruhe.de

PII S0040-1951(97)00022-X

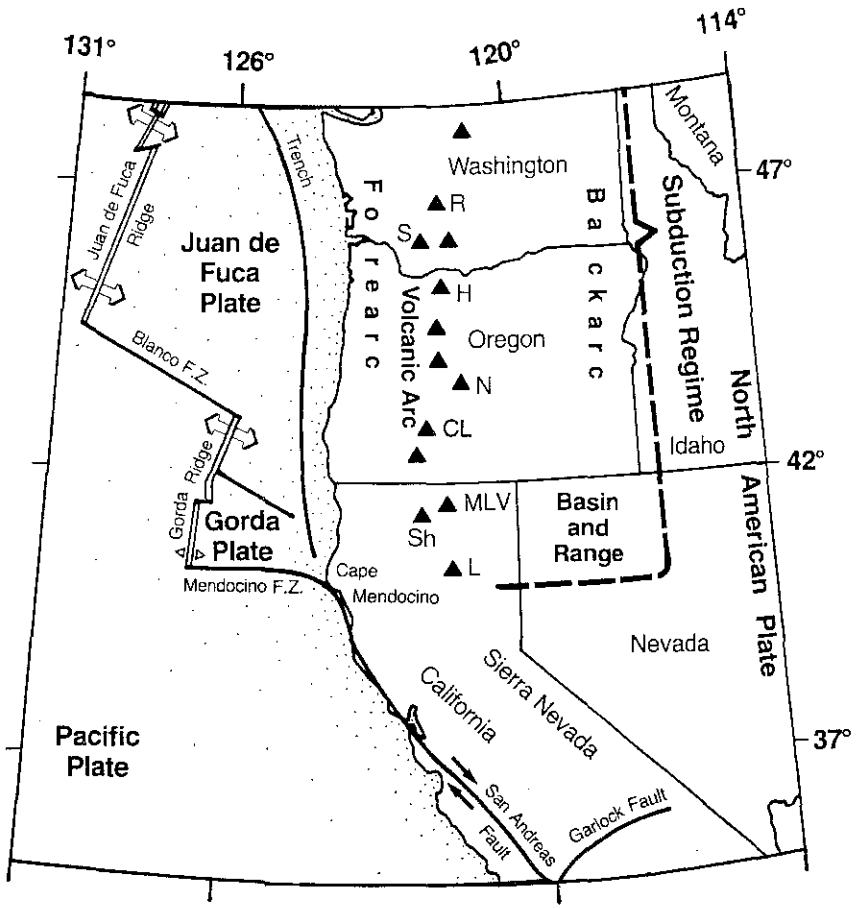

Fig. 1. Simplified tectonic map showing major tectonic provinces related to subduction in the NW United States. Medicine Lake volcano (MLV) is part of the Cascade Range, which is the volcanic arc of this subduction zone. Other prominent volcanoes are Mt. Lassen (*L*), Mt. Shasta (*Sh*), Crater Lake (*CL*), Newberry (*N*), Mt. Hood (*H*), Mt. St. Helens (*S*), and Mt. Rainier (*R*). Modified after Mooney and Weaver (1989).

fornia, Fig. 1) can be related to broad low-velocity anomalies in the upper mantle (Benz et al., 1992). During an experiment similar to the one described here, Harris et al. (1991) found a low-velocity body in the lower crust beneath Crater Lake, Oregon (CL, Fig. 1), another major Quaternary volcano of the Cascade Range. Harris et al. (1991) and Humphreys and Dueker (1994) also imaged the subducting slabs of the Juan de Fuca and Gorda plates (Fig. 1) beneath the southern Cascade Range. The magmatic arc belonging to this subduction zone is the Cascade Range. Due to the large station spacing in their study, Humphreys and Dueker (1994) could not resolve anomalies associated with the individual volcanoes.

The experiment at MLV was specifically designed to search for crustal and upper-mantle magmatism within the Geothermal Program of the U.S. Geological Survey (USGS). The recording stations were spaced 3 km apart over the crest of MLV, allowing a spatial resolution of 3–5 km in the crust, comparable to the wavelengths of the compressional waves used. Additional stations were placed at wider intervals to as much as 55 km from the summit to get information about the upper mantle directly beneath MLV (Fig. 2). This paper describes this teleseismic experiment, the data, and our modeling. Our interpretation is done with the attainable resolution in mind, as well as previously known geological and geophysical information.

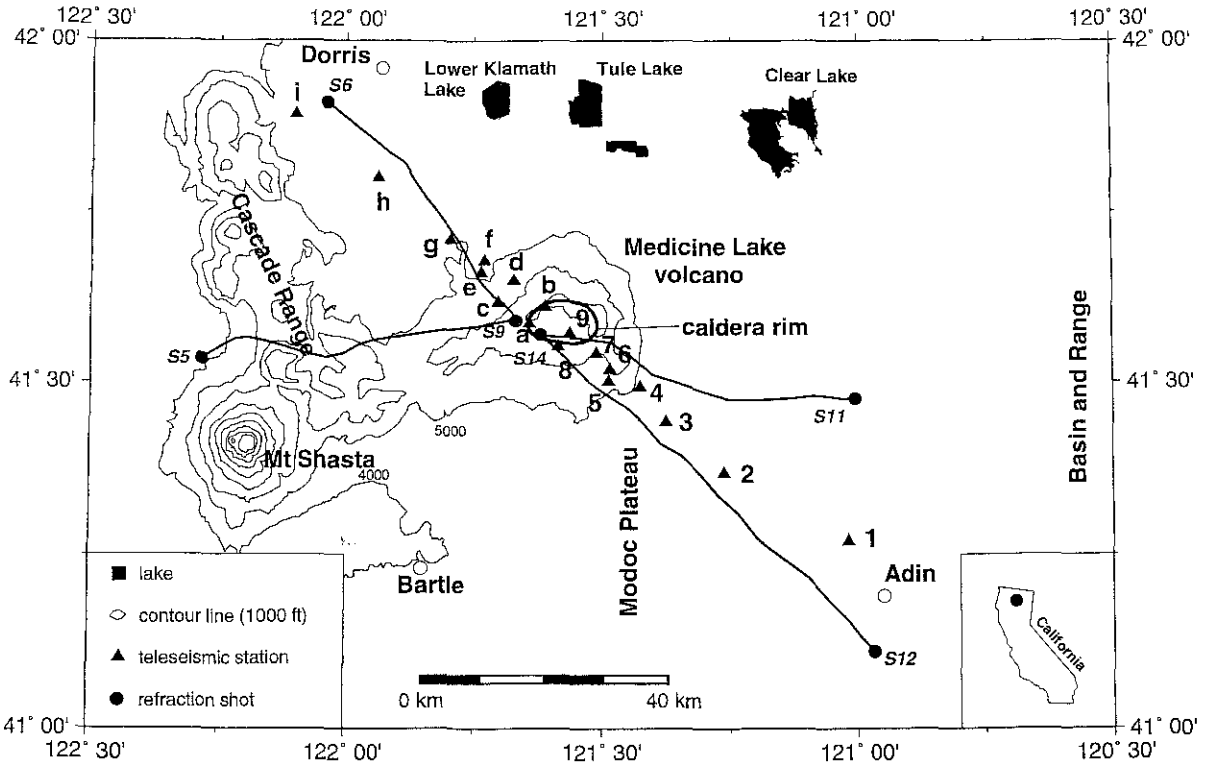

Fig. 2. Map of teleseismic stations (triangles) and seismic-refraction lines (Zucca et al., 1986) in the Medicine Lake region. Shot points of the seismic-refraction experiment are shown by dots. Elevation contours (in feet) show that Medicine Lake Volcano is east of the Cascade Range axis, on the east end of a volcanic highland connecting it to Mt. Shasta, the most voluminous stratovolcano of the Range. Inset shows the location of Medicine Lake volcano within California.

2. Geology and geophysics

Medicine Lake volcano is a Pleistocene and Holocene shield volcano. It is located on the Modoc Plateau about 50 km east of the volcanic front of the Cascade Range arc (Figs. 1 and 2) and is the most voluminous volcano of the Cascade Range (approximately 600–750 km^3 total extruded volcanic rocks) (Dzurisin et al., 1991). MLV's lavas cover an area of 2000 km^2 and their composition is primarily mafic. In and around the 7 km by 12 km summit caldera, Holocene lava flows with a total volume of 7.8 km^3 are present. The most recent eruption took place about 900 years B.P. (Donnelly-Nolan et al., 1990) demonstrating the youth of magmatic activity. Geodetic leveling results (Dzurisin et al., 1991) show subsidence rates as much as 11 mm/a for the volcano. This subsidence is interpreted to result from rapid E–W crustal extension, combined with crustal loading by the volcanic edifice, cooling and crystallization of magma, or magma withdrawal (Dzurisin et al., 1991).

The magmatic system controlling the activity at MLV has been an issue of debate (Donnelly-Nolan, 1988). Heiken (1978) proposed a small crustal magma chamber (about 10 km^3) whereas the model by Eichelberger (1981) contains a large crustal magma reservoir (140 km^3). The most recent geological model developed by Donnelly-Nolan (1988) contains a large number of small magma bodies of varying composition, reflecting different stages of magma differentiation and epochs of activity. These small reservoirs are linked, fed, and drained by many dikes and sills. A large silicic magma chamber is excluded from her model because previous geophysical results (Evans, 1982b; Stanley, 1982; Zucca et al., 1986) together with geologic data exclude at least large silicic chambers.

The resolution of our teleseismic models in the crust provides additional constraints on the presence or absence of any large, hot body (greater than 100 km^3). Geophysical data support Donnelly-Nolan's model of numerous small intrusions, but with only one active chamber in the upper 5 km of the volcano (Evans and Zucca, 1988). A local +27 mGal residual gravity anomaly over MLV was modeled as a high-density body at shallow (−0.5 to +2 km) depth (negative depth means above sea level) (Finn and Williams, 1982). Evans and Zucca (1988, 1993) find a high-velocity, normal attenuating region at −0.85 to +1.2 km depth using a high-resolution active source 3-D tomography method ('NeHT'). Two seismic-refraction profiles crossing MLV in NW–SE and E–W directions show a travel-time advance of 0.3 s at MLV (Zucca et al., 1986). This advance is modeled as a high-velocity horst-like or plug-like structure in the uppermost crust consistent with the other studies. Due to the lack of appropriate seismic phases, Moho depth could not be measured but is assumed to be 36–45 km (Zucca et al., 1986).

Chiarabba et al. (1995) confirmed the high-velocity anomaly underneath the caldera, using local seismic tomography methods with data derived from the active source experiments of Zucca et al. (1986) and Evans and Zucca (1988). Stanley et al. (1990) interpret a high-resistivity bump in the upper crust at MLV as an intrusive complex. Wang and Hansen (1990) find a positive magnetic anomaly centered at MLV and surrounded by negative values. A receiver function analysis of teleseismic waves gave an estimate of 33–36 km for crustal thickness beneath MLV (Zandt et al., 1987).

Despite the variety of studies of the upper crust, little is known about the lower crust and upper mantle underneath the Cascade Range's most voluminous volcano. The high-density, high-resistivity, high-velocity, positive magnetic anomaly feature of the upper 3 km is well resolved, whereas deeper structures remain enigmatic.

3. Teleseismic experiment and data

The field work for measuring the teleseismic arrival times was conducted by the USGS in the summer of 1981. The receiver array was deployed on a 110-km-long line centered over the caldera of MLV (Fig. 2). The NW–SE direction was chosen according to the common back-azimuths of teleseisms. The inner twelve recording units (stations 4–f; Fig. 2; Table 1) were spaced 3 km apart to enhance spatial resolution of the crust. At each end of the profile, three stations (1–3 and g–i) were placed at larger intervals to obtain crossing rays in the upper mantle beneath MLV.

Table 1
Coordinates of recording sites of the Medicine Lake experiment, 1981

Name	Latitude (°)	Longitude (°)	Elevation (m) [a]	No. records [b]
ml1	41.2693 N	121.0392 W	1939	20
ml2	41.3668 N	121.2827 W	1301	15
ml3	41.4417 N	121.3950 W	1347	18
ml4	41.4933 N	121.4485 W	1533	21
ml5	41.5007 N	121.4677 W	1698	28
ml6	41.5187 N	121.5050 W	1690	28
ml7	41.5418 N	121.5310 W	1911	18
ml8	41.5523 N	121.5655 W	2007	20
ml9	41.5722 N	121.5815 W	2057	28
mla	41.5857 N	121.6210 W	2070	24
mlb	41.6105 N	121.6300 W	2134	13
mlc	41.6168 N	121.6810 W	1820	28
mld	41.6492 N	121.6927 W	1637	24
mle	41.6608 N	121.7158 W	1533	33
mlf	41.6780 N	121.7490 W	1463	23
mlg	41.7092 N	121.8162 W	1366	14
mlh	41.8002 N	121.9575 W	1311	6
mli	41.9022 N	122.0905 W	1323	22

[a] Elevation above sea level.
[b] Number of records used in inversion.

The eighteen seismographs were USGS analog '5-day recorders' (Criley and Eaton, 1978) which were equipped with 3-component 1-Hz seismometers. During the two-month recording interval, about 70 teleseismic earthquakes were registered, plus several regional events. Hypocenter coordinates were taken from the USGS's 'Preliminary Determinations of Epicenters' bulletin. For this study, 37 teleseisms approximately along-strike with the array were selected (back-azimuths of 120°–170° and 290°–340°; Table 2; Fig. 3) yielding good coverage of ray parameters and a reversed profile. These 37 events provided 383 readings of compressional-wave phases (367 P, 9 ScP, and 7 PKPdf). Weighting factors were subjectively assigned to the data via a picking quality (111 'a'-readings, best quality; 213 'b', good; 59

Table 2
Teleseismic events used in the inversion

Location	Date (y-m-d)	Time (h:min:s)	Latitude (°)	Longitude (°)	Depth [a] (km)	m_b [b]	Dist. [c] (deg.)	BAZ [d] (deg.)	No. of records [e]
Eastern Japan	81-06-03	05:40:12.0	41.919 N	137.449 E	278	4.6	70	309	6
South Atlantic	81-06-03	05:47:44.4	35.560 S	17.040 W	10	5.8	122	110	7
Juan Fern. Islands	81-06-04	07:39:40.4	34.203 S	78.834 W	33	5.1	85	145	8
Peru	81-06-05	07:09:05.2	11.329 S	73.713 W	108	5.3	85	128	10
Aleutian Islands	81-06-05	07:09:19.1	52.281 N	165.199 W	33	5.5	31	305	9
Peru–Equador	81-06-09	23:34:54.5	3.903 S	80.709 W	37	5.3	58	130	7
Fox Islands	81-06-07	17:52:33.9	53.833 N	165.135 W	33	5.0	31	308	11
Chile–Bolivia	81-06-16	05:41:49.1	21.486 S	68.337 W	76	5.4	80	130	17
Guatemala	81-06-17	06:32:11.0	14.000 N	91.200 W	97	5.2	38	127	16
Mexico	81-06-20	03:50:03.4	16.184 N	98.472 W	22	5.0	32	135	13
North Chile	81-06-21	10:30:01.1	20.256 S	70.446 W	36	5.2	77	131	11
Peru	81-06-22	17:53:21.3	13.166 S	74.522 W	24	5.1	69	130	7
Easter Island	81-06-30	11:48:26.7	23.115 S	114.211 W	10	5.2	64	172	14
South Pacific	81-07-06	08:25:59.2	36.233 S	101.090 W	10	5.0	79	163	10
Mexico	81-07-07	06:14:20.1	13.858 N	92.228 W	50	4.7	37	128	7
Volcano Islands	81-07-10	12:33:54.2	22.756 N	144.014 E	45	5.3	78	290	9
South Pacific	81-07-10	18:02:04.9	37.216 S	95.369 W	10	5.2	82	159	5
Hokkaido	81-07-11	06:34:55.6	41.426 N	142.116 E	59	5.3	68	306	10
Alaska	81-07-12	01:27:56.3	67.707 N	161.199 W	33	5.2	33	334	7
Fox Islands	81-07-12	17:03:25.5	52.452 N	169.115 W	39	5.2	33	305	9
Andeanof Islands	81-07-13	22:10:02.4	50.207 N	173.158 W	6	5.5	36	301	12
Andeanof Islands	81-07-15	07:51:55.1	51.487 N	174.787 W	41	4.9	37	304	6
Shikoku, Japan	81-07-16	15:46:37.0	33.467 N	132.072 E	59	4.9	79	305	5
Argentina	81-07-18	11:15:18.1	22.677 S	66.238 W	246	5.0	82	130	9
Kuril Islands	81-07-19	00:58:09.9	45.425 N	150.076 E	33	5.5	61	306	9
South Honshu	81-07-19	16:52:50.4	29.738 N	142.198 E	31	5.1	75	296	6
Mexico	81-07-21	09:14:18.6	16.282 N	98.373 W	25	5.1	32	134	15
Mexico	81-07-21	09:20:10.4	16.167 N	98.491 W	41	4.8	32	135	12
Mexico	81-07-21	10:22:54.7	16.508 N	98.408 W	53	5.2	32	134	13
Peru	81-07-22	07:40:53.8	11.121 S	78.139 W	39	4.9	66	132	11
Bolivia	81-07-23	13:51:26.5	16.979 S	64.941 W	38	5.3	78	125	13
Hokkaido	81-07-28	17:00:57.5	41.676 N	139.973 E	177	5.4	69	307	9
Taiwan	81-07-30	22:59:17.0	25.639 N	123.671 E	199	5.1	90	305	10
Kamchatka	81-07-31	21:06:51.8	51.232 N	157.708 E	50	5.2	54	309	12
Alaska	81-08-01	01:42:16.4	60.136 N	153.185 W	114	5.2	27	324	8 and 9
Mexico	81-08-01	11:20:04.8	17.228 N	99.431 W	64	4.9	31	135	15
Fox Islands	81-08-02	06:40:25.6	52.600 N	168.130 W	33	4.4	33	305	16

[a] Event depth; [b] body-wave magnitude; [c] epicentral distance from array center; [d] azimuth from array center toward epicenter; [e] number of records used in inversion.

'c', fair). These weights are used in the subsequent calculations of travel-time residuals and velocity.

Absolute travel-time residuals were calculated for the Earth model of Herrin et al. (1968). Subtracting the (weighted) mean residual of each event (a static term accounting for hypocenter mislocations and distal path effects) yields 'weighted relative residuals'. In the following, weighted relative residuals are used throughout and simply called 'residuals'.

In Fig. 4 these residuals are plotted as a function of station position along the array, and subdivided by ray approach direction and incidence angle in the lowermost crust. Grey symbols indicate rays from the NW (left), black symbols are for rays approaching from the SE (right). Different symbols represent 15-degree intervals of incidence angles. These were calculated using the slownesses from the tables of Herrin et al. (1968). The residuals are not

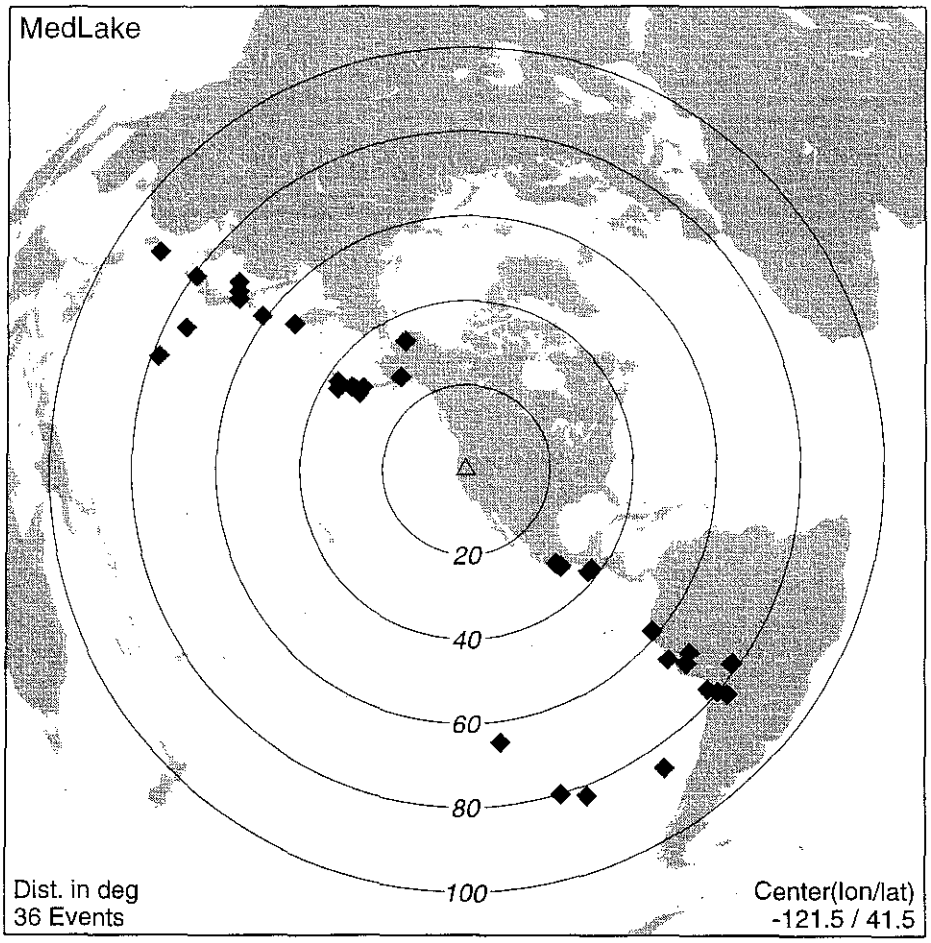
MedLake
20
40
60
80
100
Dist. in deg
36 Events
Center(lon/lat)
-121.5 / 41.5

(a)

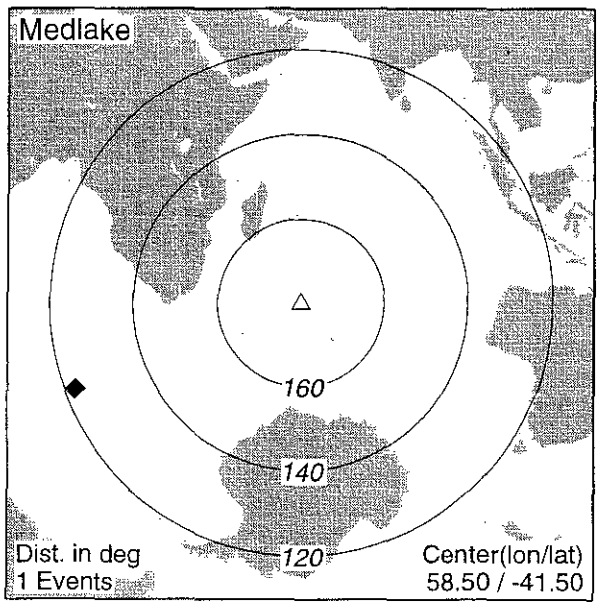
Medlake
160
140
120
Dist. in deg
1 Events
Center(lon/lat)
58.50 / -41.50

(b)

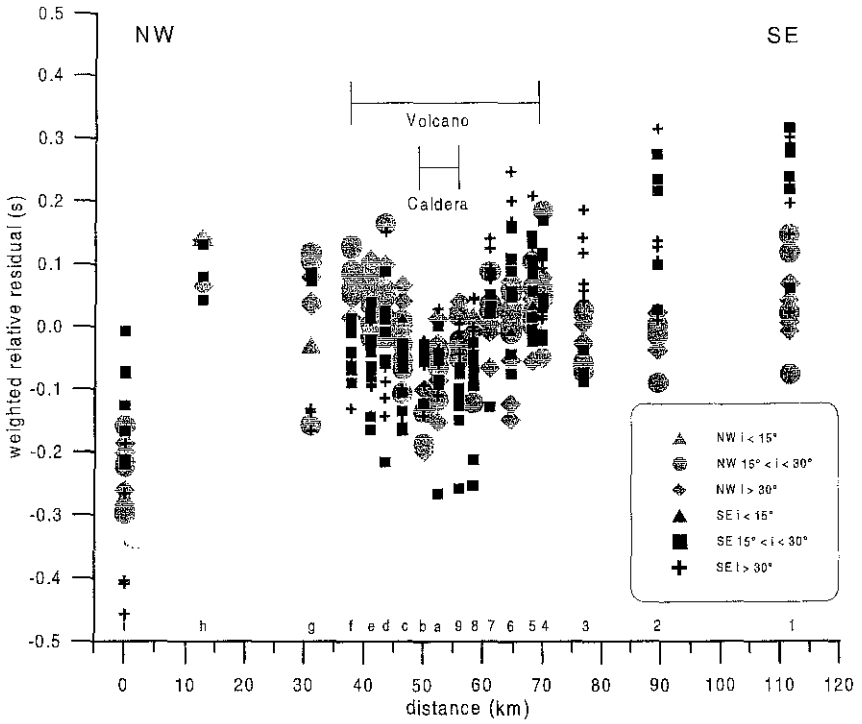

Fig. 4. Weighted relative travel-time residuals plotted as a function of distance along the linear recording array. Station indices are at the bottom and correspond to Fig. 2. Incidence angles (in the lower crust) are coded by symbols; approach direction is also indicated by grey shading vs. black.

corrected for station altitude. Maximum elevation effects are 0.1 s, principally at the center of the volcano where residuals are negative. They would be more negative with elevation corrections included.

Two main features in Fig. 4 are obvious at once. First there is a gradual increase of residuals (time delay of arrivals) from NW to SE of about 0.3 s. This pattern is partly caused by the very early arrivals at station i in contrast with h, which will be discussed in detail below. Secondly, there is a 0.15 s decrease of residuals at MLV, which is most prominent at stations inside or near the caldera (stations b, a, 9). This decrease is a minimum estimate because these stations were deployed on the highest topography found along the profile. Since the fast arrivals are present for all teleseismic back-azimuths and slownesses, they are best explained by a zone of high-velocity material inside the edifice or at shallow depth beneath the volcano. The local decrease in travel time is also observed at stations outside the caldera on the flanks of the volcano. Recording sites g–c on the NW slope of MLV show slower arrivals from the NW compared to SE arrivals, which passed through the deep parts of MLV. Similarly, stations on the SE half of the profile recorded slower arrivals from the SE while rays that passed under MLV arrive earlier. This reversing pattern is taken as evidence for a high-velocity zone at greater depth underneath MLV, a zone extending deeper than seen in previous experiments. An analysis of an early subset of these data (Evans, 1982b) yielded similar results.

The NW–SE increase in travel-time delay (~0.3

Fig. 3. Epicenter distribution of the 37 teleseisms (diamond symbols) used, in an azimuthal equidistant projection relative to the recording network at Medicine Lake volcano (triangle in a). Good coverage of events between 25° and 90° distance along the strike of the linear array is evident. (a) Distance range 0°–110°. (b) Antipode region with distance range 110°–180°.

s) is an indication that the deep compressional-wave velocity structure varies significantly along the profile. The delay in arrivals originating from the SE events at the stations in the SE part of the array (stations 1, 2, 3) can be interpreted in two ways. Either the arrivals from the NW events appear relatively fast because they are transmitted through the cold slabs of the Juan de Fuca and Gorda plates as well as any deep high-velocity material above the slabs. Or the lithosphere below the SE part of the network is itself characterized by decreased seismic velocities. The second cause for the slower velocities could be a result of the hot, extending backarc environment of the Basin and Range Province. A combined slab–backarc effect on the travel time is also possible.

The marked contrast in Fig. 4 between stations h and i is azimuth-independent and could be interpreted as a shallow structure beneath either or both stations. There is no evidence in the gravity field or the geology of station i to suggest a major high-velocity feature there. However, recent geologic mapping places station h atop a thin veneer of lava flow (less than 10 m thick) overlying poorly indurated pyroclastic deposits and, below that, probably sediments of the Butte Valley/Red Rock Valley basin (R. Christiansen, pers. commun., 1996). It is very likely, therefore, that this h/i contrast is due to shallow low-velocity material beneath station h. This interpretation implies a stronger regional trend from early arrivals at station i to late arrivals at station 1.

Subsequent sections deal with the inversion of these residuals to obtain relative-velocity images in a vertical section along the array.

4. Inversion procedure

The inversion technique used to calculate the velocity perturbations is named ACH after the authors of the original paper (Aki et al., 1977). This method assigns measured travel-time residuals to velocity perturbations in a depth range comparable to the aperture of the recording array. The target volume is parameterized into a block structure and the starting model consists of homogeneous layers (except, possibly, the shallowest layer). From each station, rays are traced through the blocks in this initial model according to the theoretical ray parameters determined after Herrin et al. (1968). The travel-time residuals are then distributed as velocity changes along the rays. This calculation uses a damped-least-squares inversion algorithm (Aki et al., 1977).

Since the introduction of the 3-D inversion method by Aki et al. (1977), several improvements in technique have been made to enhance the resolution properties of this procedure. A summary of these developments is given by Evans and Achauer (1993). Here we briefly describe the options of the inversion program that we used for the Medicine Lake data set. For mathematical details we refer to the papers of Aki et al. (1977) and Evans and Achauer (1993), which have comprehensive reference lists.

In a deviation from parameterization into rectilinear blocks, the first layer was in effect divided into independent cone-like volumes. In particular, each station was associated with a 'block' to which all rays arriving at that station were assigned. Only those arriving at that station were included. These rays sample a cone-shaped region beneath the station. Hence, each cone acts as a station 'static' to model near-surface effects.

Although the ACH method is a linear, one-step inversion, it is possible to calculate the velocity perturbations in the first layer iteratively. Using this option strong near-surface heterogeneities can be modeled and removed (Dawson et al., 1990; Evans and Achauer, 1993). This stripping technique proved to be necessary for the Medicine Lake data because of the large near-surface anomalies present.

To mitigate errors due to arbitrary positioning of block boundaries, to improve lateral resolution, and to obtain lateral smoothing, an offset-and-average technique (Evans and Zucca, 1988) was used. To enhance the vertical spatial resolution, a new method of thinning layers was applied. This technique was recently introduced and validated by Evans and Achauer (1993), who discuss it in detail and illustrate it with synthetic examples. Note that no block in such smoothed models is individually resolved, only regions comparable in size to the blocks of the base model (or more fully the 'volume metrics', which are not shown here in the interests of brevity). The principal advantage of such smoothing is in the elimination of parameterization artifacts and in easing the eye's job.

5. Modeling

Modeling of the Medicine Lake data was done in the following sequence. First a classical ACH parameterization was selected, basing block width on station spacing and making block thickness 1.5 times that width. For this 'base' model, the damping parameter was selected by comparing data fit with model complexity (Fig. 5). Then a standard ACH-inversion was performed to identify the main anomalies and produce resolution and covariance matrices. Lastly, the three techniques described in the previous section (iterative stripping, layer thinning, and offset-and-average) were applied to get a sharper picture of the deep structure beneath MLV. This is the 'smoothed, iteratively stripped' model.

We produced both a regional smoothed, iteratively stripped model, using data from all stations, and a similar crustal model, using data from only the densely spaced stations (3–g). Lastly, we produced a 'deterministically stripped' model of the mantle by removing the crustal fraction of the travel-time residuals as estimated from existing seismic-refraction models (Catchings, 1983; Zucca et al., 1986).

The regional base model (Fig. 6a) consists of two crustal layers and three mantle layers (Table 3, (a)). The first layer was treated as station statics as described above. Initial velocities were taken from Zucca et al. (1986) for the crust and Herrin et al. (1968) for the mantle. In Fig. 5 the trade-off curves used to determine the damping parameters of base models are shown. For the regional model a value of 40 $s^2/\%^2$ was chosen as a compromise between residual variance and model length (complexity). We inverted for 71 blocks each sampled by at least 5 rays. The inversion produced a variance improvement of 86.4%. In Fig. 6 the compressional-wave velocity perturbations, resolution diagonal elements, and standard errors of this inversion are displayed.

The velocity perturbations of this regional base model contain four major features. In the uppermost layer (down to 14.7 km depth) there is a clear velocity increase beneath the center of the volcano, and velocity decreases beneath the flanks of MLV (Fig. 6a). Underneath station i (at the NW end) is the

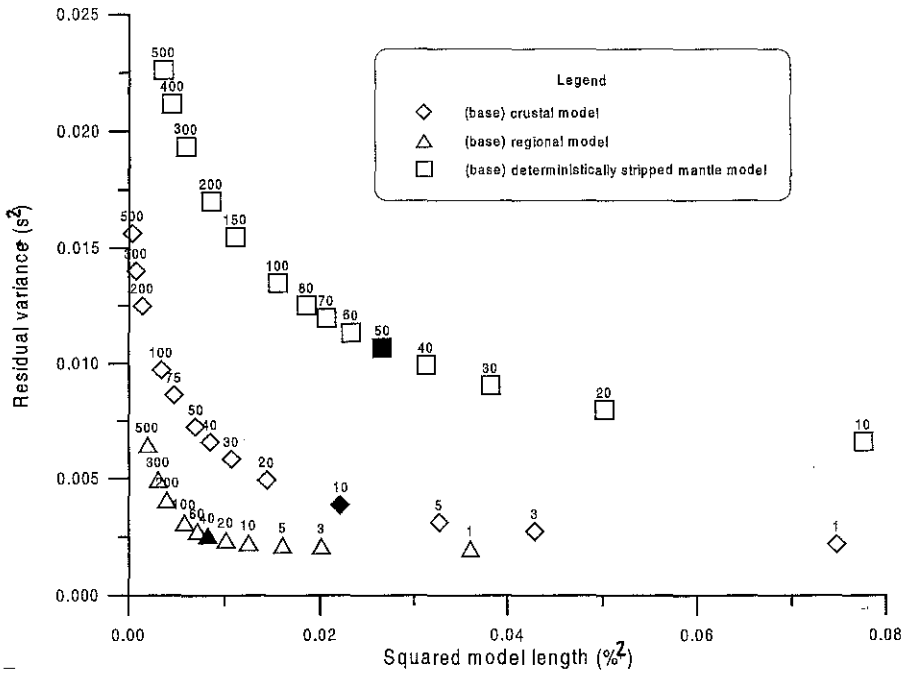

Fig. 5. 'Trade-off' curves for selecting optimal damping parameters. Data variance remaining after inversion (i.e., data misfit) is plotted against model length (i.e., complexity) for a range of damping parameters (numbers are $s^2/\%^2$ or $10^{-4} \times s^2$). Filled symbols represent the values selected for the crustal (diamonds), regional (triangles), and mantle base models (squares).

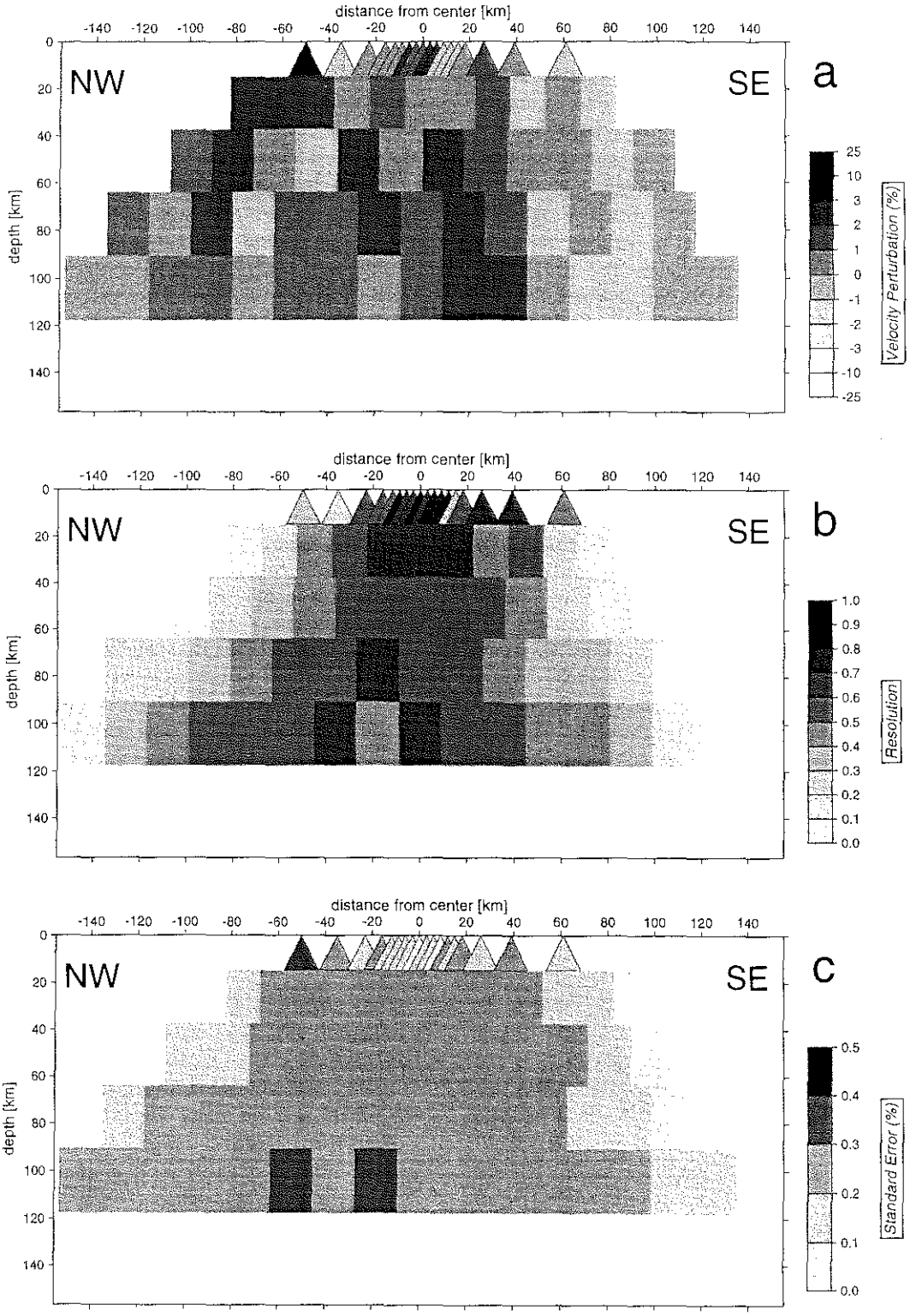

Fig. 6. Regional base ACH-model of 5 layers: (a) velocity perturbations, (b) diagonal elements of the resolution matrix, and (c) standard errors. The model center is in the middle of MLV's caldera, no vertical exaggeration.

Table 3
Model parameterizations corresponding to Figs. 6–9

Layer No.	Initial velocity (km/s)	Thickness (km)	Size: NW–SE (km)	No. of blocks NW–SE
(a) Base regional model, center: 41.58°N, 121.60°W				
1	5.10	14.7	–[a]	18
2	6.83	22.4	15.0	13
3	8.10	26.6	18.0	14
4	8.19	26.9	18.0	17
5	8.26	27.1	18.0	19
(b) Iteratively stripped and smoothed regional model. The size and the number of blocks result from the offset and averaging procedure relative to the base model in (a)				
1	3.32	1.65	–[a]	18
2	5.71	6.21	5	35
3	6.26	6.86	5	35
4	6.45	7.02	5	41
5	6.83	7.48	5	41
6	7.21	7.89	5	41
7	8.07	8.76	6	38
8	8.10	8.87	6	44
9	8.13	8.94	6	44
10	8.17	8.95	6	47
11	8.20	8.96	6	50
12	8.22	8.97	6	53
13	8.24	9.04	6	53
14	8.26	9.00	6	59
15	8.28	9.06	6	59
(c) Base crustal model				
1	2.96	1.45	–[a]	14
2	4.92	4.05	2.7	21
3	6.27	5.16	3.4	19
4	6.26	5.11	3.4	21
5	6.44	5.31	3.5	23
6	6.54	5.37	3.6	23
7	7.11	5.83	3.9	24
8	7.23	5.83	3.9	27
9	8.06	6.64	4.4	26
(d) Iteratively stripped, smoothed crustal model. The size and the number of blocks result from the offset and averaging procedure relative to the base crustal model in (c)				
1	2.44	0.35	–[a]	14
2	4.00	1.10	0.90	65
3	4.42	1.20	0.90	65
4	4.52	1.25	0.90	65
5	5.81	1.60	0.90	65
6	6.27	1.70	1.13	59
7	6.29	1.75	1.13	59
8	6.25	1.70	1.13	59
9	5.96	1.65	1.13	62
10	6.42	1.70	1.13	65
11	6.43	1.75	1.13	65
12	6.43	1.75	1.67	65
13	6.44	1.81	1.67	68
14	6.45	1.76	1.67	71
15	6.46	1.76	1.20	71
16	6.47	1.76	1.20	71
17	6.71	1.86	1.20	74
18	7.07	1.91	1.30	71
19	7.11	1.96	1.30	74
20	7.16	1.96	1.30	74
21	7.20	1.96	1.30	77
22	7.24	1.91	1.30	77
23	7.24	1.96	1.30	83
24	8.05	2.21	1.47	74
25	8.06	2.21	1.47	80
26	8.07	2.22	1.47	80
(e) Deterministically stripped, smoothed mantle model. The size and the number of blocks result from the offset and averaging procedure relative to the base model in (a)				
1	3.32	1.65	–[a]	18
2	6.50	37.50	300[b]	3
3	8.07	8.76	6	38
4	8.10	8.87	6	44
5	8.13	8.94	6	44
6	8.17	8.95	6	47
7	8.20	8.96	6	50
8	8.22	8.97	6	53
9	8.24	9.04	6	53
10	8.26	9.00	6	59
11	8.28	9.06	6	59

[a] 'Special' first layer option: one separate cone below each receiver.
[b] Crustal 'superblock' with fixed velocity (see text). Before smoothing, the 'superblock' is 900 km wide.

largest positive value in the model (+4.1%), as expected from the residuals (Fig. 4). This feature would extend further SE in a gradational manner if station h were not anomalously stowed at shallow depth, with this anomaly smearing to depth in the poorly sampled region below station i. The lower crust and the mantle directly beneath MLV are also characterized by increased seismic velocities. The SE part of the model contains generally lower seismic velocities than the NW half, particularly, if station h's effect were compensated.

In Fig. 6b, the diagonal elements of the resolution matrix are shown. As expected from the distribution of rays there is good resolution in the center of the model, especially in the crust where the ray density

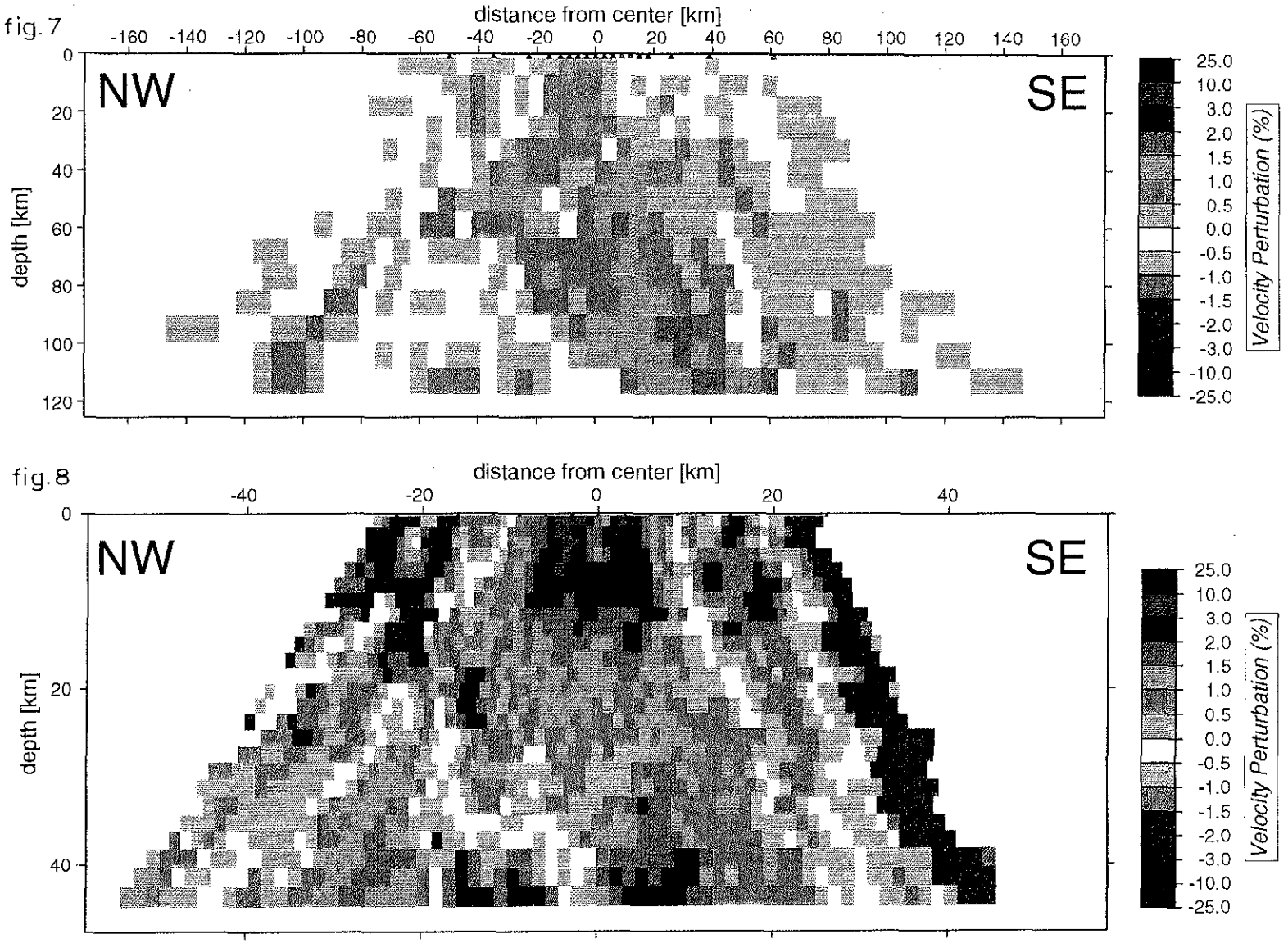

Fig. 7. Regional (smoothed, thinned, iteratively stripped) model. Compressional-wave velocity perturbations in percent. The center of the model (0 km) corresponds to the center of MLV's caldera. Parameterization (starting velocities and layer thicknesses) is in Table 3 and description of methods and resolution are in the text.

Fig. 8. Crustal (smoothed, thinned, iteratively stripped) model. Otherwise similar to Fig. 7.

is highest. The square root of the diagonal elements of the covariance matrix can be seen in Fig. 6c. These give an estimate for the standard errors of the velocity perturbations. Most standard errors lie in the interval between 0.2% and 0.3% velocity perturbation. Since the anomalies in the standard model range between 2% and 3% they are up to 10 times larger than the error bars of the inversion process due to the estimated data uncertainties.

To obtain a more detailed model with fewer parameterization artifacts, the layer-thinning method (Evans and Achauer, 1993) was applied. Layer thicknesses in the standard model were divided by three (Table 3, (b)), as well as the damping parameter to preserve a constant regularization proportion for the inversion algorithm. In addition, horizontal smoothing was induced by a lateral offset-and-average procedure (Evans and Zucca, 1988; Evans and Achauer, 1993). In our study, three offsets along the horizontal axis were performed and the three models averaged in block-overlap areas. We know of no way to compute meaningful resolution and covariance matrices directly for offset-and-average models or a meaningful covariance matrix for thinned-layer models (Evans and Achauer, 1993). We refer the reader to the base model for the latter (Fig. 6b, c).

Because these inversion results do not show major differences from the base model, the errors in the thinned-layer model cannot be much larger than displayed in Fig. 6c.

The final modeling step was iterative stripping of near-surface effects. This procedure also removes most of the regional anomaly because that anomaly is essentially unresolvable in depth. Velocity perturbations in the 1.65-km-thick first layer were calculated iteratively until changes in successive steps became less than 1% (e.g., Dawson et al., 1990). After 18 iterations this convergence was achieved, yielding a perturbation range of −13.6% (stations 2 and h) to +22.3% (station i). The values for all stations are listed in Table 4. The range of the seismic velocity perturbations appears to be reasonable for a complex lithological structure like a volcano, with lava flows, intrusive crystalline rocks, and pyroclastic layers, subsumed with the broad regional gradient probably caused by deeper structure.

The final stripped, smoothed, regional model is displayed in Fig. 7. Due to the iterative stripping, the amplitude of the velocity perturbations decreased slightly compared to the base model. This effect occurs because smearing from strong near-surface heterogeneities into the deeper layers and from the regional gradient into all depths are largely suppressed by the stripping. The main features of the base model (Fig. 6a) are readily identified in this stripped, smoothed regional model (Fig. 7). The spatial distribution of the anomalies is better defined in Fig. 7, because the block parameterization no longer constrains the anomalies.

An iteratively stripped, smoothed crustal model also was calculated (Fig. 8). Only data from the inner fourteen stations (stations 3–g, Fig. 2), which are at about 3-km intervals, were used (312 observations). Using a base crustal model of nine layers (Table 3, (c)), the damping parameter (Fig. 5) was determined to be optimal at 10 $s^2/\%^2$. The variance improvement of this inversion was 79.9%. Layer thinning,

Table 4
Compressional-wave velocity perturbations in the shallowest layer of the iteratively and deterministically stripped regional models (Figs. 7 and 9) and the iteratively stripped crustal model (Fig. 8) (values are given in percent deviation from the initial velocity, see Table 3)

Station No.	Iteratively stripped regional model (18 iterations)	Deterministically stripped regional model (7 iterations)	Iteratively stripped crustal model (11 iterations)
1	−1.36	11.41	–[a]
2	−13.58	−22.11	–[a]
3	−6.09	−13.88	−14.01
4	−7.37	−8.52	−11.34
5	−5.57	−1.97	−6.24
6	−6.94	−6.83	−9.00
7	1.06	5.34	2.35
8	11.23	14.20	14.14
9	13.53	16.80	18.06
a	13.70	24.21	20.37
b	16.08	24.69	22.60
c	6.35	20.12	11.51
d	−5.30	−6.80	−6.72
e	−7.21	−14.74	−9.27
f	−7.89	−15.14	−10.07
g	−7.92	−21.48	−11.78
h	−14.10	−6.55	–[a]
i	22.33	2.26	–[a]

[a] Data from these stations are not used in the inversion for the crustal model.

offset-and-average, and iterative stripping were applied as for the regional model. Parameterization is described in Table 3, (d). To reduce smearing from the mantle, three thin mantle layers (Nos. 24–26, Table 3, (d)) were added beneath the estimated Moho to absorb most of the signal from deeper regions.

The general pattern of velocity perturbations seen in this crustal model (Fig. 8) agrees with the crustal part of the regional model (Fig. 7). Details are discussed in the next section.

For the Medicine Lake teleseismic profile there is the rare benefit of having a nearly coincident seismic-refraction profile (Fig. 2). Details of the seismic-refraction experiment and its interpretation can be found in Catchings (1983), Zucca et al. (1986), and Fuis et al. (1987). Of interest here is the crustal compressional-wave velocity structure along the NW–SE striking line, with shot points S6, S9, and S12 (Fig. 2). It provides good control of the upper part of the crust down to about 20 km depth. The lower crust is less well defined and the mantle not at all. The same holds for the E–W line (shots S5, S14, and S11) which crosses the NW–SE refraction line and the teleseismic profile within MLV's caldera. The interpretations of both refraction lines contain a shallow high-velocity body beneath MLV to explain an observed local travel-time advance of up to 0.3 s (Zucca et al., 1986). We used this refraction model for our 'deterministic' crustal stripping procedure by assuming a flat Moho at 37 km depth. This choice is consistent with another, longer regional model of the Cascade Range (Leaver et al., 1984) as well as a receiver function analysis at MLV (Zandt et al., 1987).

Synthetic teleseismic travel times through this modified refraction model were calculated using RAY84PC (Thybo and Luetgert, 1990). Ray tracing started at the base of the crust and the starting angle was determined using the theoretical ray parameter for the individual events (j) after the standard earth model by Herrin et al. (1968). At the stations (i), the travel time was interpolated between nearest neighboring rays. Computational errors within the given velocity model were less than 0.02 s (compared with teleseismic reading errors of 0.05 s). The synthetic crustal travel times $t_{i,j}^{\text{obs,crust}}$, were then subtracted from the observed total travel times $t_{i,j}^{\text{obs,total}}$ to obtain travel-times which would be measured at the Moho. The theoretical travel times $t_{i,j}^{\text{theo}}$ of Herrin et al. (1968) were similarly reduced to Moho by tracing rays through the Herrin crustal model to a depth of 37 km:

$$t_{i,j}^{\text{obs,corr}} = t_{i,j}^{\text{obs,total}} - t_{i,j}^{\text{obs,crust}} \quad (1)$$

$$t_{i,j}^{\text{theo,corr}} = t_{i,j}^{\text{theo,total}} - t_{i,j}^{\text{theo,crust}} \quad (2)$$

The corrected teleseismic travel times $t_{i,j}^{\text{obs,corr}}$ and $t_{i,j}^{\text{theo,corr}}$ were used to calculate weighted relative residuals that would be observed at the crust–mantle boundary. Using these corrected data, a 'pure' mantle model was determined as if the velocity structure of the crust was known. The parameterization of this mantle model (Table 3, (e)) is largely the same as for the regional model except that most of the crust is subsumed in a single, very large block to minimize the travel-time perturbation absorbed by the model in that depth range. This large crustal 'superblock' also keeps ray tracing reasonably accurate through the crust.

An iteratively calculated first layer was included to strip specific site statics for each receiver (Table 4). This step is necessary because near-surface anomalies directly beneath the stations are not resolved by the seismic-refraction model (station siting is not identical). Taking a base model with three mantle layers, the damping parameter was chosen to be 50 $s^2/\%^2$ (Fig. 5). Lastly, layer thinning and offset-and-average were applied to the mantle layers.

The result is shown in Fig. 9. The distribution of the velocity perturbations does not vary significantly from the regional (crust included) model of Fig. 7 but the amplitudes are slightly higher. This difference is unsurprising because the deterministically stripped model (Fig. 9) does not subsume deeper, regional structure as happens in iterative stripping (Fig. 7). The fit to the data is good, with a variance improvement of 81.3%.

We are aware that correction for the crustal travel times has the following uncertainties. The Moho depth was not measured along the profile and is poorly constrained. The seismic-refraction input model is biased by subjective modeling, and anisotropy is not accounted for (teleseismic rays travel about perpendicularly to seismic-refraction waves). Details of very shallow structure, such as

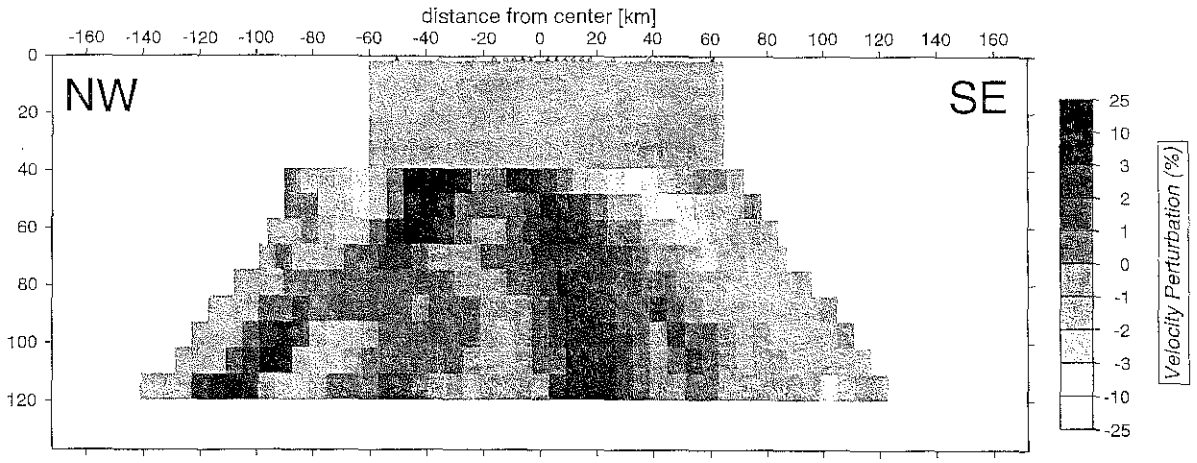

Fig. 9. Deterministically stripped mantle model. Otherwise similar to Fig. 7. The seismic velocity in the crustal 'superblock' has not changed (0% perturbation); it is assumed that this part of the medium was removed completely by the deterministic stripping procedure, which was based on a seismic-refraction model.

the possible basin beneath station h, will vary between the refraction line and the teleseismic stations. Lastly, the resolving power of the two methods varies in differing patterns from one another along the profile. However, we believe that the principal crustal features are contained in the refraction model and that the stripping procedure eliminates the gross crustal velocity anomalies.

6. Results

The iteratively stripped regional model (Fig. 7) contains the same major features described above for the regional base model (Fig. 6a). Due to the iterative stripping procedure, the 1.65-km-thick first layer of the regional model contains large velocity perturbations (Table 4). These large perturbation values beneath stations 1, 2, h and i are due to local geology and not related to MLV, because the recording sites were located far off the volcano. The perturbation values in Table 4 show the same overall trend for the three different models, except for station 1. Cones beneath stations at the center of the volcano show high seismic velocities (up to +24.7%) and those on the flanks have low seismic velocities (as low as −21.5%).

Underneath MLV the iteratively stripped regional and crustal models (Figs. 7 and 8) contain increased velocities. In that crustal model (down to 15 km depth), the upper crust has up to 10% faster compressional-wave velocity beneath the caldera than in the surrounding crustal material (Fig. 8). Below 20 km depth, the contrast decreases to about 5% but remains significant. The three mantle layers at the bottom of the crustal model absorb most deeper structure and should not be interpreted.

In the deeper models (iteratively and deterministically stripped regional models, Figs. 7 and 9), the mantle contains a zone of increased seismic velocity underneath MLV. This anomaly dips SE and it is more spatially coherent in the iteratively stripped regional model (Fig. 7) than in the deterministically stripped model (Fig. 9). In the former, the mantle is clearly characterized by slower seismic velocity in the SE than in the NW. This is in accordance with the regional trend of the residuals in Fig. 4, though the depth of the effect is largely unresolved. For the most part, the mantle anomalies have the same overall distribution in Fig. 7 and in Fig. 9. However the anomalies in Fig. 9 are larger in amplitude by roughly 1.5%.

Since the biggest anomalies occur directly beneath the Moho in Fig. 9 (40–50 km depth), there may be smearing of incompletely removed crustal velocity anomalies into the mantle. This smearing particularly affects the deeper crustal high-velocity material beneath MLV, which is not contained in the seismic-refraction model.

7. Interpretation and discussion

7.1. Crust

In the upper crust beneath MLV there is no sign of an active, hot magma chamber, which probably would be imaged as a low-velocity anomaly. On the contrary, a zone of increased seismic velocity dominates from the top of the model (Table 4) to the Moho with decreasing velocity contrasts at depth (Fig. 8). If the low velocities in the crust NW and SE of MLV are interpreted as 'normal' background, then the total velocity increase below the caldera in the upper 10 km is as much as 10%. This interpretation of the velocity contrast underneath the flanks makes sense because the least-squares algorithm is constrained to produce about as much high- as low-velocity perturbation within the model; calculated velocities are relative to the mean and absolute velocities are unknown. In addition, this effect is local and can create the appearance of a 'moat' of low around a high, or vice versa (e.g., fig. 13.8a of Evans and Achauer, 1993). In our crustal model (Fig. 8) this 'moat' effect is likely. The existence of a high-velocity body beneath the caldera is seen in the data (see above and Fig. 4) and is also known from other geophysical investigations (Finn and Williams, 1982; Catchings, 1983; Evans and Zucca, 1988). On the other hand these studies did not reveal adjacent crustal lows. We infer that the 'lows' at the NW and SE edges are not isolated features but typical background for this region. Though this background is a porous stack of Miocene and younger basalt and interbedded sediment, we do not infer increased temperature or active magmatism. Our velocity contrast of 10% is of the same order as in the seismic-refraction model by Zucca et al. (1986). Increased seismic velocity under a large active volcano is also known from other teleseismic tomography studies. At Kilauea volcano, Hawaii, Ellsworth and Koyanagi (1977) found an anomaly with increased P-wave velocity (maximum contrast 17%) underneath the summit complex and two radial rift zones, compared to surrounding nonrift upper crust. Stauber et al. (1988) demonstrate crustal high-velocity very similar to MLV beneath Newberry volcano, Oregon (Fig. 1). Newberry is geologically very similar to MLV.

The +10% anomaly in the upper crust beneath MLV can be explained as a region of cold, solidified intrusive rocks. Due to the wavelength of the teleseismic phases, our technique is not capable of resolving single small intrusive bodies. The multiple-intrusion model of Donnelly-Nolan (1988) is consistent with our crustal model, if the high-velocity anomaly represents the average seismic velocity increase caused by mainly solidified mafic material within parent crustal rock (probably Sierra Nevada basement; Fuis et al., 1987). A hot magma reservoir, the size of Eichelberger's (1981) model, is ruled out by our data, but a large, subsolidus pluton could be present. The small upper-crustal low-velocity anomaly found by Evans and Zucca (1988) and confirmed by Chiarabba et al. (1995) is not detected by our data, presumably because it is slightly NE of our teleseismic profile and in any case is to small to be resolved. The model presented here is consistent with the seismic-refraction studies (Catchings, 1983; Zucca et al., 1986; Fuis et al., 1987).

The large velocity contrast between stations h and i is interpreted as a combination of the regional, fast to the NE, anomaly and a local sedimentary basin anomaly beneath h.

7.2. Upper mantle

The positive velocity deviation of +2% to +3% (from mean) in the upper mantle directly beneath MLV corresponds to roughly 0.15 to 0.25 km/s increase in absolute P-velocity. Although this high-velocity feature dips SE, it is not likely to be part of the subducting Gorda plate. The actively subducting plate is at about 100 km depth at this longitude in northern California (Walter, 1986) and becomes steeply dipping east of Mt. Shasta (D. Stauber, pers. commun., ca. 1990). The possibility remains that it is a cut-off steeply dipping fragment of subducting plate, but we know of no other suggestion for such a plate fragment in northeastern California, and would expect it to have detached and sunk if present.

There are, therefore, four models that can explain this high-velocity anomaly: variations in temperature, melt fraction, composition, and/or seismic anisotropy. Anisotropy might explain the feature if upward melt flow aligned mantle minerals differently from the subduction and back-arc processes. However, we lack both a model predicting such flow

alignments and S birefringence data to test the hypothesis. It remains a viable interpretation, though speculative.

It might be thought that the high-velocity material is the residuum of a fractional melting process that fed MLV's volcanic activity. To test this possibility we looked at the depths of 40 and 80 km, assuming an anhydrous lherzolitic mantle (a lherzolitic composition of the mantle beneath MLV has been proposed by Bartels et al., 1991). As starting composition and in-situ conditions we chose a spinel–lherzolite (40 km depth) and a garnet–lherzolite (80 km depth), lithostatic pressure of 1.1 and 2.5 GPa and various possible temperatures (1000–1400°C). Fractional melting with removal of the melt fraction will preferentially reduce the spinel (Spi), garnet (Gt), and clinopyroxene (CPx) content, yielding a harzburgitic residuum consisting of olivine (Ol) and orthopyroxene (OPx) (Hall, 1987). The calculated P-velocity (V_p) in such mantle rocks, using the method of Voigt–Reuss–Hill (Hill, 1952), is not significantly greater than that of the starting mineralogical composition, simply because the minerals with high P-wave velocity (Spi and Gt) are removed preferentially. The increase in Ol and OPx content offsets this effect, but not enough to increase V_p until very large melt fractions are reached (>15%). This result assumes the same pressure and temperature conditions for the starting composition and the residuum. In this case the decrease in Fe/Mg ratio, which increases V_p, is accompanied by the decrease in Al content which reduces V_p. Further calculations using the method of Sobolev and Babeyko (1994) demonstrate that both effects mutually compensate each other and no significant change in V_p in the peridotite facies can be expected (Sobolev et al., 1996). Results for a hydrous mantle are similar.

The temperature effect on V_p in peridotites can also be estimated. If one keeps the lherzolitic composition fixed, then the high-velocity anomaly can be explained as a region 200°C to 250°C colder than the surrounding mantle (cf. Tittgemeyer et al., 1995), if anharmonicity (Anderson, 1988) and anelasticity (Karato, 1993) are included. This result is based on the same compositional and pressure parameters as above. Therefore the high-velocity zone might represent a volume cooled in some manner by MLV volcanism, removing heat to the surface.

Alternatively, removal of a small melt fraction from a partial melt can explain the anomaly mechanically, by increasing the shear strength of the rock. A +3% velocity contrast implies removal of about 3% melt fraction (Mavko, 1980) from a rock of unknown but small melt fraction assumed to underlie the whole region. Using the geometry of the high-velocity region in the regional model (Fig. 7) and extrapolating it in three dimensions as a cylindrical body, a total volume of 90,000 km^3 is derived. The volume of the above-mentioned 3% melt, that would have left the mantle, is consequently on the order of 2700 km^3 with only a fraction (~30%) of this reaching the surface. Even less melt (1% to 2%) would have to be removed from the mantle if some of the partial melt were originally distributed in planar blebs, as has been found in more recent work described by Faul et al. (1994).

In short, MLV volcanism presumably has removed heat and melt from the upper mantle. Temperature changes and mechanical stiffening due to melt removal are a plausible combination for explaining the MLV high-velocity upper-mantle anomaly. The continuation of the anomaly to 120 km depth suggests that the magmatism of MLV originates at least partly from the lower lithosphere. Unfortunately our data set is not appropriate to speculate further on the lithosphere/asthenosphere boundary region.

There is also a velocity contrast on larger scales between the SE and NW parts of our mantle models (Figs. 4, 7 and 9). This broad velocity contrast is at least 1% to 2% (with the MLV mantle anomaly overprinting another 1% to 2% in the SE-dipping feature). This difference may simply be the contrast between Basin and Range mantle southeast of MLV and Cascadian mantle northwest of MLV. Hearn et al. (1991) found a similar variation in V_p of 0.1 to 0.2 km/s at sub-Moho depth with a tomography study of Pn-phases in the same area that we study. The regional trend is also consistent with the signature of an east-dipping subducting slab and back arc. In particular, it is very similar in magnitude, location, and azimuth independence to the back-arc portion of the anomaly described by Harris et al. (1991), from a similar, linear array passing through Crater Lake (CL, Fig. 1). Their profile also show transitions to the Basin and Range Province in the back arc SE of Crater Lake, so it is in nearly identical terrain to our

own study. The velocity gradient may in part reveal a progressive down-dip (eastward) assimilation of the subducted slab. Given that the Basin and Range also contrasts with adjacent back-arc material to the north (Iyer et al., 1982), both intra- and above-slab effects probably are present. Our study lacks the depth resolution of this regional anomaly needed to shed light on the distinction.

However, the velocity contrast again implies a temperature, melt fraction, anisotropy, or compositional difference along our array. The temperature contrast hypothesis is explored using the technique of interpreting seismic velocity perturbations in terms of temperature and degree of partial melt which includes effects of anharmonicity, anelasticity, mineral reactions and partial melt (cf. Sobolev et al., 1997). In the depth range of 60 to 100 km, a 2% velocity contrast implies a 170–240°C temperature contrast for dry mantle, or less than 150°C for a wet mantle. If a temperature of 1400°C (asthenosphere) in the Basin and Range is used, then the temperature under the Cascades would be 1200–1250°C, which is plausible. However, the other explanations also remain viable, in particular a contribution from the subducted slab, and awaits addition of S-velocity and Q information or other data.

The interpretation of the crustal and regional tomography models (Figs. 7 and 8) is summarized and displayed in Fig. 10 as an interpretative cross-section. The high-velocity anomaly in the lithosphere is indicated as a continuous feature from the surface down to 120 km depth. Melt and heat removal from the lithospheric mantle are assumed to have been proceeded through magmatic processes. The basaltic magmas intrude the crust and form a zone with increased seismic velocity after solidifying. Because the SE-dipping high-velocity zone reaches to at least 120 km depth, we expect that at least some of the melts have their origin in the lower lithosphere. The lateral variations of V_p in the mantle are represented

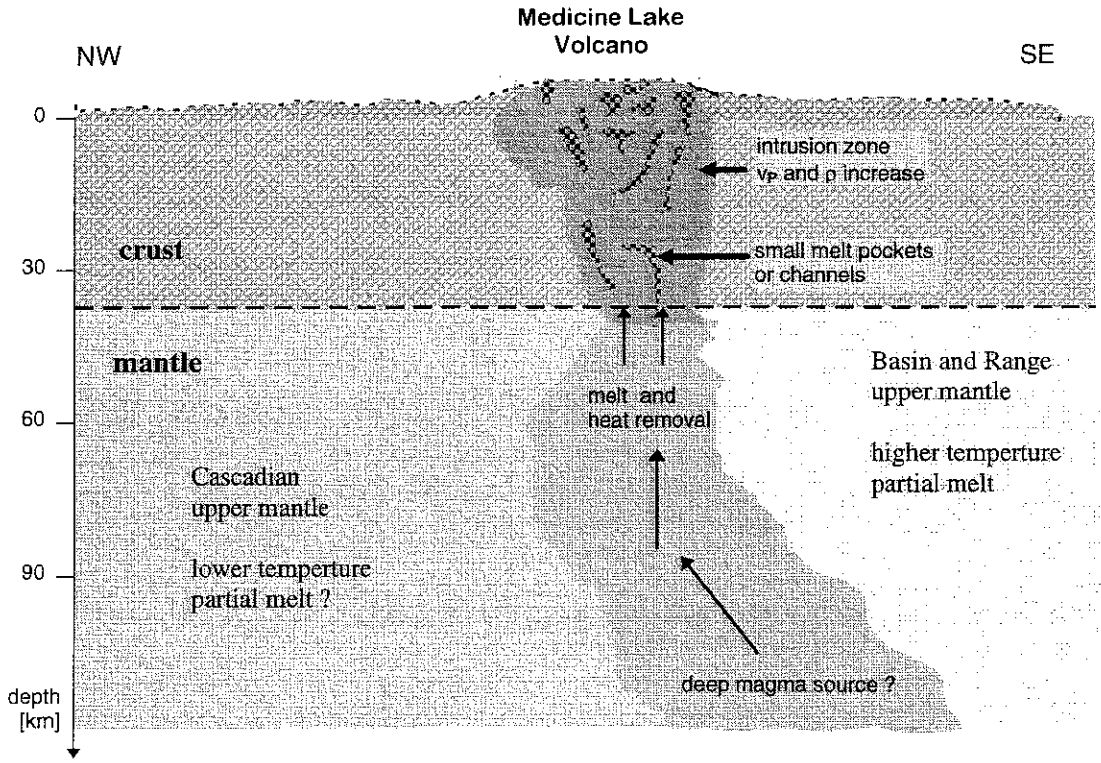

Fig. 10. Combined interpretative cross-section for the teleseismic crustal and regional models. The crust beneath MLV contains numerous mostly subsolidus intrusions that increase the average P-velocity. In the uppermost mantle P-velocity variations are explained by differences in temperature and melt fraction (increased temperature or melt fraction is indicated with lighter grey).

with different shades of grey in Fig. 10. The light shaded region in the SE corresponds to a mantle regime with decreased average V_p (−1%) interpreted to result from increased temperatures and presence of partial melt. The Cascadian mantle shown in darker grey is characterized by slightly faster average V_p (+0.5%) due to lower ambient temperature.

8. Conclusions

The 1981 teleseismic survey of MLV and adjacent areas provided excellent data to constrain the compressional-velocity structure of the upper 120 km of the lithosphere. It reveals that the Cascade Range's most voluminous volcano does not have a large, active magma chamber in the crust. Additionally there is little evidence of upwelling hot material in the mantle beneath MLV. Our crustal and regional models show increased seismic velocities in the crust (up to +10%) and in the mantle (+3%) beneath the volcano (Fig. 7). A sketch which summarizes our interpretation is shown as Fig. 10. For the crust we infer that the high-velocity zone is largely due to solidified remnants of the magmas which led to the formation of this shield volcano. For the mantle, the effects of melt and heat removal are proposed. The crustal structure we resolve is consistent with extant seismic-refraction models (Fuis et al., 1987). In the mantle, our regional model and the deterministically stripped model both contain a broad gradient in velocity, −1% to −2% in the SE compared to the NW. This asymmetry could be the contrasting signature between the uppermost mantle beneath the Cascades (NW) and the backarc environment or the Basin and Range Province (SE) with or without a contribution from structure in the underlying subducted slab. The Basin and Range Province is characterized by increased temperatures (Lachenbruch and Sass, 1977), reduced Pn velocity (Hearn et al., 1991), and thinned crust (Prodehl, 1970), so lower velocity at depth is unsurprising.

Acknowledgements

We would like to thank Julie Donnelly-Nolan, Karl Fuchs, Ruth Harris, and Stephan Sobolev for fruitful discussions. Stephan Sobolev provided preprints and petrophysical calculations. H. Dres, M. Jordan, F. Lange, and B. Schechinger helped prepare the figures. Several figures were greatly improved by the GMT system of Wessel and Smith (1991). P. Davis and an anonymous reviewer gave helpful suggestions. One of the authors (J.R.) was sponsored by the Deutsche Forschungsgemeinschaft (SFB 108). J.R.'s stay in Menlo Park at USGS was supported by a USGS exchange visitor program through W. Mooney. USGS work and the original field study were supported by the USGS Geothermal Studies Program, and initiated and guided by H.M. Iyer. This paper is SFB 108 contribution No. 582 and contribution No. 714 of the Geophysical Institute of the University of Karlsruhe.

References

Aki, K., Christofferson, A. and Husebye, E.S., 1977. Determination of the three-dimensional seismic structure of the lithosphere. J. Geophys. Res., 82: 277–296.

Anderson, D.L., 1988. Temperature and pressure derivatives of elastic constants with application to the mantle. J. Geophys. Res., 93: 4688–4700.

Bartels, K.S., Kinzler, R.J. and Grove, T.L., 1991. High pressure phase relations of primitive high-alumina basalts from Medicine Lake volcano, northern California. Contrib. Mineral. Petrol., 108: 253–270.

Benz, H.M., Zandt, G. and Oppenheimer, D.H., 1992. Lithospheric structure of northern California from teleseismic images of the upper mantle. J. Geophys. Res., 97: 4791–4807.

Catchings, R.D., 1983. Crustal Structure from Seismic Refraction in the Medicine Lake Area of the Cascade Range and Modoc Plateau, Northern California. MSc Thesis, University of Wisconsin–Madison, 182 pp.

Chiarabba, C., Amato, A. and Evans, J.R., 1995. Variations on the NeTH high-resolution tomography method: a test of technique and results for Medicine Lake volcano, northern California. J. Geophys. Res., 100: 4035–4052.

Criley, E. and Eaton, J., 1978. Five-day recorder seismic system. U.S. Geol. Surv., Open-File Rep., 78-266, 85 pp.

Dawson, P.B., Evans, J.R. and Iyer, H.M., 1990. Teleseismic tomography of the compressional wave velocity structure beneath the Long Valley region, California. J. Geophys. Res., 95: 11,021–11,050.

Donnelly-Nolan, J.M., 1988. A magmatic model of Medicine Lake volcano, California. J. Geophys. Res., 93: 4412–4420.

Donnelly-Nolan, J.M., Champion, D.E., Miller, C.D., Grove, T.L. and Trimble, D.A., 1990. Post-11,000-year volcanism at Medicine Lake volcano, Cascade Range, northern California. J. Geophys. Res., 95: 19,693–19,704.

Dzurisin, D., Donnelly-Nolan, J.M., Evans, J.R. and Walter, S.R., 1991. Crustal subsidence, seismicity, and structure near Medicine Lake volcano, California. J. Geophys. Res., 96: 16,319–16,333.

Eichelberger, J.C., 1981. Mechanism of magma mixing at Glass Mountain, Medicine Lake highland volcano, California. In: D.A. Johnston and J.M. Donnelly-Nolan (Editors), Guides to Some Volcanic Terranes in Washington, Idaho, Oregon, and Northern California, U.S. Geol. Surv., Circ., 838: 183–189.

Ellsworth, W.L. and Koyanagi, R.Y., 1977. Three-dimensional crust and mantle structure of Kilauea volcano, Hawaii. J. Geophys. Res., 82: 5379–5394.

Evans, J.R., 1982a. Compressional wave velocity structure of the upper 350 km under the eastern Snake River plain near Rexburg, Idaho. J. Geophys. Res., 87: 2654–2670.

Evans, J.R., 1982b. Compressional-wave velocity structure of the Medicine Lake volcano and vicinity from teleseismic relative traveltime residuals. Techn. Prog. Abstr. and Biog., 50th SEG Annual Meeting and Exposition, Dallas, expanded abstract, pp. 482–485.

Evans, J.R. and Achauer, U., 1993. Teleseismic velocity tomography using the ACH method: theory and application to continental-scale studies. In: H.M. Iyer and K. Hirahara (Editors), Seismic Tomography: Theory and Practice. Chapman and hall, London, pp. 319–360.

Evans, J.R. and Zucca, J.J., 1988. Active high-resolution seismic tomography of compressional wave velocity and attenuation structure at Medicine Lake volcano, northern California Casacade Range. J. Geophys. Res., 93: 15,016–15,036.

Evans, J.R. and Zucca, J.J., 1993. Active source high-resolution (NeTH) tomography: velocity and Q. In: H.M. Iyer and K. Hirahara (Editors), Seismic Tomography: Theory and Practice. Chapman and Hall, London, pp. 695–732.

Faul, U.H., Toomey, D.R. and Waff, H.S., 1994. Intergranular basaltic melt is distributed in thin, elongated inclusions. Geophys. Res. Lett., 21: 29–32.

Finn, C. and Williams, D.L., 1982. Gravity evidence for a shallow intrusion under Medicine Lake volcano, California. Geology, 10: 503–507.

Fuis, G.S., Zucca, J.J., Mooney, W.D. and Milkereit, B., 1987. A geologic interpretation of seismic-refraction results in northeastern California. Geol. Soc. Am. Bull., 98: 53–65.

Hall, A., 1987. Igneous Petrology. Longman, Harlow, 573 pp.

Harris, R.A., Iyer, H.M. and Dawson, P.B., 1991. Imaging the Juan de Fuca plate beneath southern Oregon using teleseismic P-wave residuals. J. Geophys. Res., 96: 19,879–19,889.

Hearn, T., Beghoul, N. and Barazangi, M., 1991. Tomography of the western United States from regional arrival times. J. Geophys. Res., 96: 16,369–16,381.

Heiken, G., 1978. Plinian-type eruptions in the Medicine Lake highland, California, and the nature of the underlying magma. J. Volcanol. Geotherm. Res., 4: 375–402.

Herrin, E., et al., 1968. Seismological tables for P-phases. Bull. Seismol. Soc. Am., 58: 1193–1241.

Hill, R., 1952. The elastic behaviour of a crystalline aggregate. Proc. Phys. Soc. London, Sect. A, 65: 349–354.

Humphreys, E.D. and Dueker, K.G., 1994. Western U.S. upper mantle structure. J. Geophys. Res., 99: 9615–9634.

Iyer, H.M. and Dawson, P.B., 1993. Imaging volcanoes using teleseismic tomography. In: H.M. Iyer and K. Hirahara (Editors), Seismic Tomography: Theory and Practice. Chapman and Hall, London, pp. 466–492.

Iyer, H.M., Rite, A. and Green, S.M., 1982. Search for geothermal heat sources in the Oregon Cascades by means of teleseismic P-residual technique. Techn. Prog. Abstr. and Biog., 50th SEG Annual Meeting and Exposition, Tulsa, expanded abstract, pp. 479–482.

Karato, S., 1993. Importance of anelasticity in the interpretation of seismic tomography. Geophys. Res. Lett., 20: 1623–1626.

Lachenbruch, A.H. and Sass, J.H., 1977. Heat flow in the United States and the thermal regime of the crust. In: J.H. Heacook (Editor), The Earth's Crust. Am. Geophys. Union, Geophys. Monogr., 20: 626–675.

Leaver, D.S., Mooney, W.D. and Kohler, W.M., 1984. A refraction study of the Oregon Cascades. J. Geophys. Res., 89: 3121–3134.

Lutter, W.J., Roberts, P.M., Thurber, C.H., Steck, L., Fehler, M.C., Stafford, D.G., Baldridge, W.S. and Zeichert, T.A., 1995. Teleseismic P-wave image of crust and upper mantle structure beneath the Valles caldera, New Mexico: initial results from the 1993 JTEX passive array. Geophys. Res. Lett., 22: 505–508.

Mavko, G.M., 1980. Velocity and attenuation in partially molten rocks. J. Geophys. Res., 85: 5173–5189.

Mooney, W.D. and Weaver, C.S., 1989. Regional crustal structure and tectonics of the Pacific coastal states; California, Oregon, and Washington. In: L.C. Pakiser and W.D. Mooney (Editors), Geophysical Framework of the Continental United States. Geol. Soc. Am., Mem., 172: 129–162.

Prodehl, C., 1970. Seismic refraction study of crustal structure in the western United States. Geol. Soc. Am. Bull., 81: 2629–2646.

Ritter, J.R.R., Fuchs, K., Kaspar, T., Lange, F.E.I., Nyambok, I.O. and Stangl, R.L., 1995. Seismic images illustrate the deep roots of the Chyulu Hills volcanic area, Kenya. Eos, 76: 273–278.

Sobolev, S.V. and Babeyko, A.Y., 1994. Modeling of mineralogical composition, density and elastic wave velocities in anhydrous magmatic rocks. Surveys in Geophysics, 15: 515–544.

Sobolev, S.V., Zeyen, H., Stoll, G., Werling, F., Altherr, R. and Fuchs, K., 1996. Upper mantle temperatures from teleseismic tomography of the French Massif Central including effects of composition, mineral, reactions, anharmonicity, anelasticity and partial melt. Earth Planet. Sci. Lett., 139: 147–163.

Sobolev, S.V., Zeyen, H., Granet, M., Stoll, G., Achauer, U., Bauer, C., Werling, F., Altherr, R. and Fuchs, K., 1997. Upper mantle temperatures and lithosphere–asthenosphere system beneath the French Massif Central constrained by seismic, gravity, petrologic and thermal observations. In: K. Fuchs, R. Altherr, B. Müller and C. Prodehl (Editors), Stress and Stress Release in the Lithosphere — Structure and Dynamic Processes in the Rifts of Western Europe. Tectonophysics, 275: 143–164 (this volume).

Stanley, W.D., 1982. A regional magnetotelluric survey of the Cascade mountains region. U.S. Geol. Surv., Open-File Rep., 82–126.

Stanley, W.D., Mooney, W.D. and Fuis, G.S., 1990. Deep crustal structure of the Cascade Range and surrounding regions from seismic refraction and magnetotelluric data. J. Geophys. Res., 95: 19,419–19,438.

Stauber, D.A., Green, S.M. and Iyer, H.M., 1988. Three-dimensional P velocity structure of the crust below Newberry volcano, Oregon. J. Geophys. Res., 93: 10,095–10,107.

Thybo, H. and Luetgert, J., 1990. RAY84PC: Two-Dimensional Raytracing — Synthetic Seismogram Calculation on Personal Computers. Copenhagen University, 42 pp.

Tittgemeyer, M., Ritter, J.R.R., Sobolev, S.V. and Fuchs, K., 1995. Limits of integrated petrological–seismic modelling of the lithospheric mantle. Ann. Geophys., 13, Supp. I, C114.

Walter, S.R., 1986. Intermediate-focus earthquakes associated with Gorda plate subduction in northern California. Bull. Seismol. Soc. Am., 76: 583–588.

Wang, X. and Hansen, R.O., 1990. Inversion for magnetic anomalies of arbitrary three-dimensional bodies. Geophysics, 55: 1321–1326.

Wessel, P. and Smith, W.H.F., 1991. Free software helps map and display data. Eos, 72: 441–446.

Zandt, G., Taylor, S.R. and Ammon, C.J., 1987. Analysis of teleseismic waveforms for structure beneath Medicine Lake volcano, northern California. Seismol. Res. Lett., 58: 34.

Zucca, J.J., Fuis, G.S., Milkereit, B., Mooney W.D. and Catchings, R.D., 1986. Crustal structure of northeastern California. J. Geophys. Res., 91: 7359–7382.